Multibeam ptychography with synchrotron hard X-rays

doi: 10.1364/OE.378083

Research Article Vol. 28, No. 2 / 20 January 2020 / Optics Express 1216
Optics EXPRESS

Multibeam ptychography with synchrotron hard X-rays

MAKOTO HIROSE,[1,2] TAKAYA HIGASHINO,[1,2] NOZOMU ISHIGURO,[2,3] AND YUKIO TAKAHASHI[1,2,3,*]

[1]Graduate School of Engineering, Osaka University, 2-1 Yamada-oka, Suita, Osaka, Japan
[2]RIKEN SPring-8 Center, 1-1-1 Kouto, Sayo-cho, Sayo, Hyogo, Japan
[3]Institute of Multidisciplinary Research for Advanced Materials (IMRAM), Tohoku University, 2-1-1, Katahira, Sendai, Miyagi, Japan
*ytakahashi@tohoku.ac.jp

Abstract: We report the first demonstration of multibeam ptychography using synchrotron hard X-rays, which can enlarge the field of view of the reconstructed image of objects by efficiently using partially coherent X-rays. We measured the ptychographic diffraction patterns of a Pt test sample and MnO particles using three mutually incoherent coherent beams with a high intensity that were produced by using both the multiple slits and a pair of focusing mirrors. We successfully reconstructed the phase map of the samples at a spatial resolution of 25 nm in a field of view about twice as wide as that in the single-beam ptychography. We also computationally simulated a feasible experimental setup using random modulators to further enlarge the field of view by increasing the number of available beams. The present method has the potential to enable the high spatial resolution and large field-of-view observation of specimens in materials science and biology.

1. Introduction

The emergence of third-generation synchrotron light sources enables the practical use of coherent beams in the hard X-ray region. One of the important applications is X-ray ptychography, which is a scanning variant of the coherent X-ray diffraction imaging method used to observe extended specimens [1,2]. A specimen is laterally scanned with a step separation smaller than the incident beam size, and multiple coherent X-ray diffraction patterns are recorded. The data redundancy of the diffraction dataset enables the robust reconstruction of a complex-valued sample and wave field functions via iterative phasing methods [3,4]. The achievable spatial resolution of X-ray ptychography is determined by the angular extent of the diffracted wave. Therefore, the resolution limit imposed by the fabrication accuracy of the X-ray lens can be overcome. Highly focused hard X-ray beams are useful for collecting large-angle diffraction data with a high signal-to-noise ratio [5–8]. Focused X-ray ptychography has provided high spatial resolution images in materials science and biological applications [9].

A currently daunting task in X-ray ptychography is to realize a high spatial resolution and a large field of view, which have a trade-off relationship. To achieve this task, it is essential to improve the coherent flux in synchrotron radiation. However, this is technically difficult in the hard X-ray region owing to the low coherent/incoherent ratio of synchrotron light sources. To alleviate the stringent coherence requirement in ptychography, the mixed-state reconstruction algorithm has been proposed [10], which greatly relaxed the coherence requirement and enabled the realization of dynamic imaging [11] and on-the-fly scan measurement [12,13]. However, although this algorithm allows us to efficiently use coherent X-rays in synchrotron radiation [14], the coherent fluence limits the spatial resolution and/or field of view of X-ray ptychography [6].

Multibeam ptychography is a promising approach for markedly improving the available coherent flux, which uses multiple spatially separated coherent beams that are mutually incoherent or

#378083 https://doi.org/10.1364/OE.378083
Journal © 2020 Received 17 Sep 2019; revised 11 Dec 2019; accepted 13 Dec 2019; published 8 Jan 2020

Optics EXPRESS

coherent. Multibeam ptychography is more dose efficient for high resolution and wide field of view imaging when compared with ptychography using partially coherent beams since the coherent fraction contributes to improve the spatial resolution [14]. Multibeam ptychography was first demonstrated in the visible light region [15], in which the image reconstruction was performed by an algorithm based on the information multiplexing [16]. A subsequent paper also described visualization using multiple mutually coherent beams with autocorrelation filtering [17]. Note that the coherent fluence does not limit the field of view of multibeam ptychography. Multibeam ptychography using synchrotron X-rays should be useful for improving the field of view of the reconstructed images.

In this study, we demonstrate multibeam X-ray ptychography using an undulator source in SPring-8. First, we develop an optical system installed with both multiple slits and a pair of focusing mirrors, which can provide multiple mutually incoherent coherent beams with a high intensity. Then, we measure ptychographic diffraction patterns of a Pt test sample and MnO particles and reconstruct images of both the sample and the probe. Finally, we present further improvement of multibeam ptychography using random modulators by computer simulation.

2. Principle of multibeam X-ray ptychography

Multibeam ptychography with synchrotron X-rays uses multiple spatially separated beams, which are themselves fully coherent but mutually incoherent. The exit wave ψ_n can be written by $\psi_n(\mathbf{r}) = P_n(\mathbf{r}) \cdot O_n(\mathbf{r})$ under the multiplicative approximation, where P_n is the probe function from the nth slit with the separation $\Delta\mathbf{r}_n$ and O_n is the object function illuminated by the nth probe P_n. The far-field diffracted wave field Ψ_n is derived by $\Psi_n(\mathbf{k}) = F[\psi_n(\mathbf{r})]$, where F is the Fourier transform operator. Therefore, the diffraction intensity I obtained when using N mutually incoherent coherent beams is expressed as

$$I(\mathbf{k}) = \sum_{n=1}^{n=N} |F[\psi_n(\mathbf{r})]|^2 \tag{1}$$

The iterative phasing method of multibeam X-ray ptychography aims to simultaneously reconstruct the complex transmission function O_n and the multiple probe functions P_n from the diffraction dataset. The update order of the sample scanning position and probe mode is randomly changed at each iteration. At the jth iteration, diffracted waves at the detector plane $\Psi_{n,j}$ are constrained by the measured diffraction intensity I as follows:

$$\Psi'_{n,j}(\mathbf{k}) = \frac{\sqrt{I(\mathbf{k})}}{\sqrt{\sum_{n=1}^{n=N} |\Psi_{n,j}(\mathbf{k})|^2}} \Psi_{n,j}(\mathbf{k}) \tag{2}$$

Next, the updated functions $\Psi'_{n,j}$ are back-propagated to the sample plane to obtain $\psi'_{n,j}$. In the real-space, the object and probe functions are updated as follows:

$$O_{n,j+1}(\mathbf{r}) = O_{n,j}(\mathbf{r}) + \alpha \frac{P^*_{n,j}(\mathbf{r})}{P_{n,max}} \{\psi'_{n,j}(\mathbf{r}) - \psi_{n,j}(\mathbf{r})\} \tag{3}$$

$$P_{n,j+1}(\mathbf{r}) = P_{n,j}(\mathbf{r}) + \beta \frac{O^*_{n,j}(\mathbf{r})}{O_{n,max}} \{\psi'_{n,j}(\mathbf{r}) - \psi_{n,j}(\mathbf{r})\} \tag{4}$$

where α and β are the feedback parameters, $P_{n,max} = \max\left(|P_{n,j}(\mathbf{r})|^2\right)$, and $O_{n,max} = \max\left(|O_{n,j}(\mathbf{r})|^2\right)$. In addition, a smoothness constraint based on the total variation (TV) [18] of the sample function

Optics EXPRESS

is applied to facilitate the convergence of the multibeam phasing method [19] as follows:

$$O_n'(\mathbf{r}) = \arg\min_{O_n} |\Psi_n'(\mathbf{k}) - F[P_n(\mathbf{r}) \cdot O_n(\mathbf{r})]|_{l_2} + \lambda |O_n(\mathbf{r})|_{TV} \tag{5}$$

where λ is a regularization parameter, $|\cdot|_{l_2}$ is the l_2 norm, and $|\cdot|_{TV}$ is the TV norm. These processes are performed at every scanning points and repeated until convergence is reached.

3. Experimental and reconstruction methods

A multibeam X-ray ptychography experiment was performed in the SPring-8 BL29XUL beamline [20]. Figure 1(a) shows the experimental setup. The incident X-ray was monochromatized to 6.5 keV by a Si (111) double-crystal monochromator located 43 m downstream of the light source. Multiple slits were positioned 52 m downstream of the X-ray source, which acted as secondary source. According to the van Cittert–Zernike theorem, the transverse coherence length in a slit position was 17 μm (in the horizontal direction, H) × 800 μm (in the vertical direction, V), respectively. Figure 1(b) shows a scanning ion microscopy (SIM) image of the multiple slits, which were made in a 50-μm-thick Pt film using a focused ion beam (FIB). The opening of each hole was 10 μm (H) × 30 μm (V), which was smaller than the transverse coherence length. The spacing between adjacent holes was 110 μm, which was much larger than the transverse coherence length in the horizontal direction. The number of beams was controlled by a variable-size slit positioned immediately before the multiple slits. A pair of Kirkpatrick–Baez (KB) focusing mirrors (JTEC Corporation) were placed 48 m downstream of the multiple slits, whose acceptance was 284 μm (H) × 315 μm (V). Figure 1(c) shows the focal profiles in the horizontal direction, which were measured by the dark-field knife-edge scan method when the multiple slits were adjusted to a single hole or three holes, from which the beam spacing $\Delta\mathbf{r}_n$ was determined. The full width at half maximum (FWHM) size of each focal profile was 630 nm in the horizontal direction, and the interval between the focal spots was 2.3 μm. On the other hand, the FWHM size of the focal profile was 650 nm in the vertical direction. The intensities

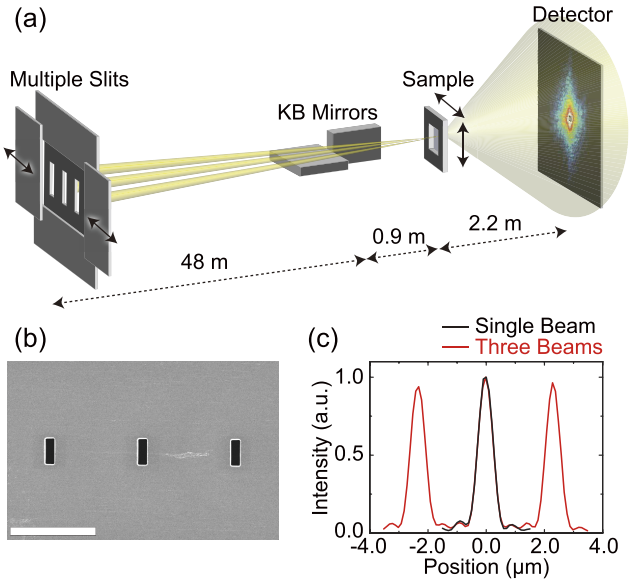

Fig. 1. (a) Schematic of multibeam X-ray ptychography experiment at SPring-8. (b) SIM image of the multiple slits. The scale bar represents 100 μm. (c) Focal intensity profiles in the horizontal direction using the single beam and three beams. The beam spacing in the three beams depends on the demagnification factor of the horizontal focusing mirror.

Optics EXPRESS

of the focal position for the single slit and three slits were 4.99×10^8 photons/s and 1.49×10^9 photons/s, respectively, which increased almost proportionally to the number of slits.

As the samples, a Pt test pattern and MnO particles were prepared. The Pt test pattern was fabricated using an FIB onto a 1-μm-thick Pt film deposited on a 500-nm-thick Si_3N_4 membrane chip, whereas the MnO particles were dispersed in ethanol solution and added dropwise on another 500-nm-thick Si_3N_4 membrane. The samples were observed by field-emission scanning electron microscopy (FE-SEM) before the ptychographic measurements.

In the ptychographic measurements, each sample was mounted on nanopositioning piezoelectric stages in a vacuum chamber with a pressure of less than 0.1 Pa, and was positioned in the focal plane. An ion chamber was inserted between the mirror and the sample to monitor the intensity fluctuation of the incident beams. The Pt test pattern was raster-scanned at 6 (H) $\times$ 25 (V) points with a step width of 300 nm and an exposure time of 10.0 s using the single beam and three beams, whereas the MnO sample was raster-scanned at 6 (H) $\times$ 20 (V) points with a step width of 300 nm and an exposure time of 5.0 s using the three beams. The diffraction patterns were recorded at each scan position by an in-vacuum pixelated detector (EIGER 1M, Dectris) with a pixel size of 75 μm that was placed 2.22 m downstream of the sample. In this experimental setup, the pixel size in the real-space image was 12.5 nm. To increase the dynamic range of the diffraction intensities, a 176-μm-thick semitransparent Si beamstop (intensity transmittance of less than 0.01 for 6.5 keV X-rays) was placed in front of the detector.

In the iterative phase retrieval calculation, the iteration was continued for up to 2900 cycles. TV regularization was applied every 300 iterations, in which the two-step iterative shrinkage/thresholding (TwIST) algorithm with the TV for the regularizer [21] was applied. The regularization parameter was optimized through the evaluation of the reciprocal-space error E_{reci} defined as follows:

$$E_{reci} = \frac{\sum_{\mathbf{k},\mathbf{a}} \left| \sqrt{I(\mathbf{k},\mathbf{a})} - \sqrt{\sum_{n=1}^{n=N} |\Psi_{n,rec}(\mathbf{k},\mathbf{a})|^2} \right|^2}{\sum_{\mathbf{k},\mathbf{a}} I(\mathbf{k},\mathbf{a})} \tag{6}$$

where $\Psi_{n,rec}$ represents the reconstructed wave field at the detector plane and $\mathbf{a}$ represents the scan coordinate.

4. Results

Figure 2(a) shows an FE-SEM image of the Pt test pattern and a schematic of the scanning points for each beam. Figure 2(b) shows the diffraction patterns of the Pt test sample obtained using the single beam and three beams. Figure 2(c) shows the reconstructed images of the Pt test pattern for the single beam and three beams. The characters are clearly visualized in both reconstructions. The field of view for the three beams is about twice as wide as that for the single beam. The field of view in the multibeam reconstruction is not proportional to the beam number. In the three beams reconstruction, the field of view for each beam partially overlaps to each other since the side peaks of the focused beams highly contribute to the image reconstruction. Here, the raster-scan geometry in X-ray ptychography likely generates periodic artefact [4], which is observed in the the single beam reconstruction. On the other hand, the artefact disappears in the three beams reconstruction. This is because the partial overlap of the field of view for the multiple beams is helpful to break the symmetry of the raster-scan. Figures 2(d) and 2(e) show the reconstructed probes for the single beam and three beams. The wave fields of the three beams, which are independently reconstructed, are similar to each other. The wavefront similarity caused the deterioration of the convergence, resulting in some low frequency artefact appear in the three beams reconstruction. Next, using the reconstructed functions of both the sample and the three mutually incoherent beams, the diffraction pattern at the illumination position in Fig. 2(b) was calculated, as shown in Fig. 2(f), which was in good agreement with the measured

Optics EXPRESS

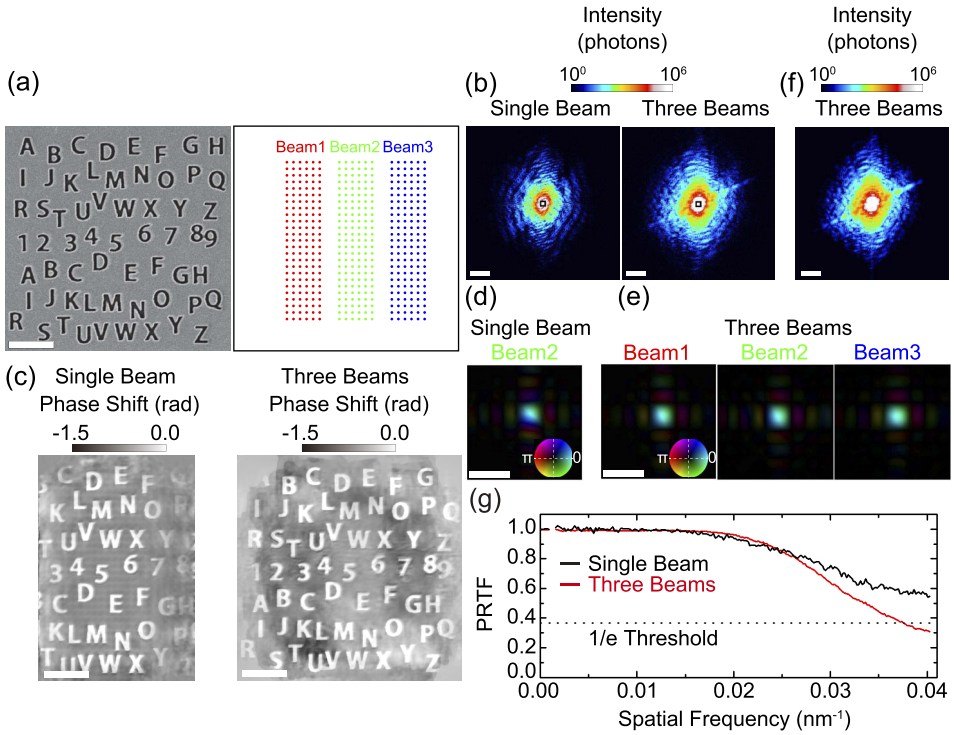

Fig. 2. (a) FE-SEM image of the Pt test sample and schematic of scanning points for each beam. The scale bar represents 2 μm. (b) Diffraction patterns of the Pt test sample obtained using the single beam and three beams. Part of the central area of the diffraction patterns is missing owing to the edge of the Si attenuator. The scale bars represent 10 μm^{-1}. (c) Reconstructed images of the Pt test sample for the single beam and three beams. The scale bars represent 2 μm. (d) Reconstructed probe for the single beam measurement. The scale bar represents 2 μm. (e) Reconstructed probe for the three beams measurement. The scale bar represents 2 μm. (f) Diffraction pattern calculated from the reconstructed images. (g) PRTF curves of the reconstructed sample images for the single beam and three beams. The full-period spatial resolution can be determined by the intersection of 1/e threshold.

pattern. According to the Eq. (6), the reciprocal-space error was 2.79×10^{-4} in the three beams reconstruction. The small error indicates the validity of the incoherence assumption of the multibeam. By phase retrieval transfer function (PRTF) analysis, the spatial resolution was determined to be 25.0 nm for the single-beam reconstruction and 26.7 nm for the three beams reconstruction in Fig. 2(g). The resolution was not significantly degraded using the three beams. Multibeam X-ray ptychography enlarged the field of view by efficiently using the synchrotron light source.

Figure 3(a) shows an FE-SEM image of the MnO particles and a schematic of the scanning points. Figure 3(b) shows the reconstructed image for the three beams. The shapes of the individual particles are in good agreement with the FE-SEM image. The spatial resolution of the MnO particles was determined to be 25.0 nm by PRTF analysis. High-efficiency imaging with a large field of view was demonstrated even on a specimen with complex structures.

Optics EXPRESS

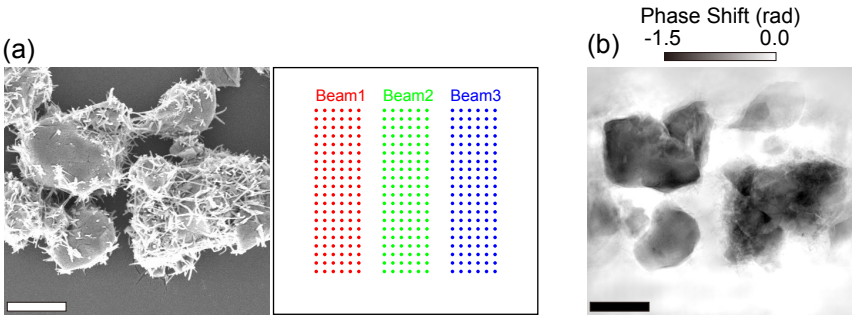

Fig. 3. (a) FE-SEM image of the MnO particles and schematic of scanning points for each beam. (b) Reconstructed image of the MnO particles for the three beams. All the scale bars represent 2 μm.

5. Discussion

In the above experiment, the small acceptance of the focusing device limited the number of available beams. However, the size of the incident beam in the multiple slits was 1.6 mm in the horizontal direction in the SPring-8 BL29XUL beamline, and therefore it is technically possible to produce more than 10 beams and/or beam spacing larger than 2.3 μm using a large-acceptance mirror. With increasing number of beams, it is concerned that the convergence of the phase retrieval calculation will deteriorate owing to the similarity of the probe function. To improve the convergence of the phase retrieval calculation, random modulators might [22,23] be useful owing to the nonsimilarity of the probe function among the beams. Random modulators might be also useful for removal of the low frequency artefact observed as shown in Fig. 2(c).

The usefulness of modulators in multibeam ptychography was evaluated by computer simulation. The simulated setup was similar to the present experimental conditions: X-rays of 6.5 keV were two-dimensionally focused by KB mirrors to a 510 nm spot as shown in Fig. 4(a), a sample was scanned at 6×25 points with a step width of 300 nm, and the beam separation was 2.2 μm. The sample was a mixture of 8-bit-depth standard pictures, and the contrast was assumed to be proportional to the Ta sample thickness up to 200 nm. The maximum phase shift was 0.41 rad. One of the calculated diffraction patterns without modulator is presented in Fig. 4(b). Each modulator consisted of a 500-nm-thick Au plate with 100-nm-diameter random through holes. When using the random modulators, the sample was placed 500 μm downstream of the modulators and the wave propagation between the sample and the modulators was calculated by the angular spectrum method. Figures 4(c) and 4(d) show the incident probe function with the modulator and the diffraction pattern, respectively. Iteration was continued for up to 2000 cycles, in which TV regularization was applied every 300 iterations.

Figure 4(e) shows the beam number dependence of the reconstructed error with/without the random modulators in multibeam X-ray ptychography, in which the reconstructed error is defined in the real-space E_{real} as follows:

$$E_{real} = \frac{\sum_{\mathbf{r}} |O(\mathbf{r}) - \gamma O_{rec}(\mathbf{r})|^2}{\sum_{\mathbf{r}} |O(\mathbf{r})|^2} \tag{7}$$

$$\gamma = \frac{\sum_{\mathbf{r}} O(\mathbf{r}) \cdot O^*_{rec}(\mathbf{r})}{\sum_{\mathbf{r}} |O_{rec}(\mathbf{r})|^2} \tag{8}$$

where $O_{rec}(\mathbf{r})$ represents the reconstructed object function. Without the modulator, the error markedly increased when the number of beams was increased from four to five. On the other hand, with the modulator, the image was successfully reconstructed even when the number of

Optics EXPRESS

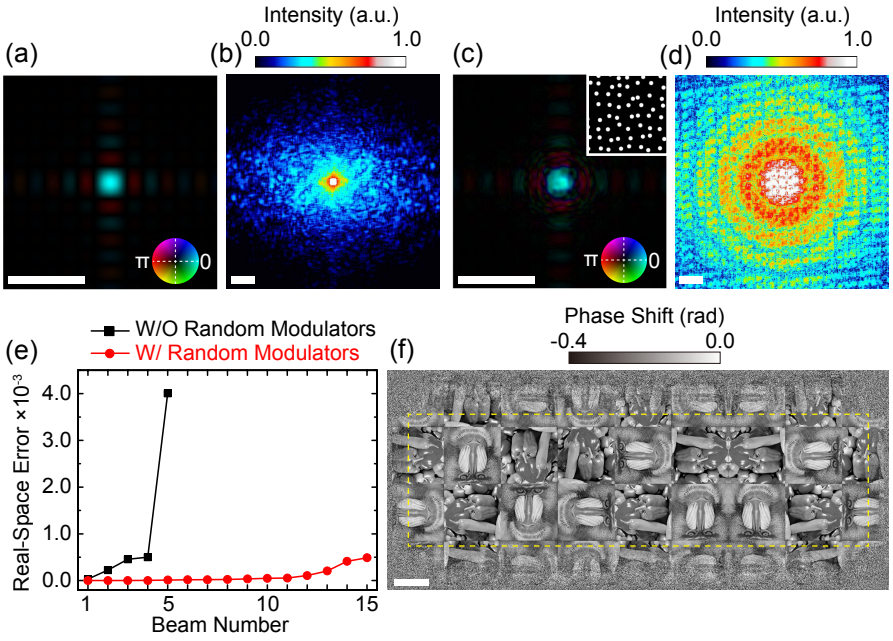

Fig. 4. (a) Incident wave field without the modulator. (b) Diffraction pattern obtained using four beams without modulators. (c) Incident wave field with the modulators. (d) Diffraction pattern obtained using 11 beams with the modulator. (e) Beam number dependence of the real-space error of the reconstructed image with/without random modulators in multibeam X-ray ptychography. (f) Reconstructed images for 11-beam with the modulator. The dashed region in the sample image was used for calculating the real-space error. All the scale bars in the real-space represent 2 μm, and all the scale bars in the reciprocal-space represent 10 μm^{-1}.

beams reaches eleven, as presented in Fig. 4(f). Furthermore, the real-space error only slowly increased when there were 11 beams. In the future, modulators will allow us to use synchrotron X-rays with a higher efficiency in multibeam X-ray ptychography and to provide larger field of view.

6. Conclusion

We have experimentally demonstrated multibeam ptychography using partially coherent X-rays at SPring-8. We developed an optical system installed with both multiple slits and a pair of KB focusing mirrors, which can provide multiple mutually incoherent coherent beams with a high intensity. Ptychographic diffraction patterns of a Pt test pattern and MnO particles were measured using a single beam and three beams. The images were successfully reconstructed at a spatial resolution of 25.0 nm. The field of view for the three beams reconstruction was about twice as wide as that for the single beam reconstruction. At present, the small acceptance of the focusing device limits the number of available beams. Using random modulators and mirrors with a large acceptance, the number of available beams in multibeam ptychography can be increased to eleven. We believe that multibeam ptychography using synchrotron X-rays has the potential to enable the high spatial resolution and large field of view observation of specimens in materials science and biology.

Optics EXPRESS

Funding

Japan Society for the Promotion of Science (JP17J01673, JP18H05253, JP19H05814); Ministry of Education, Culture, Sports, Science and Technology (Dynamic Alliance for Open Innovation Bridging Human, Environment and Materials).

Acknowledgments

We thank T. Ishikawa and K. Endo for many stimulating discussions, as well as Y. Kohmura for his help in the synchrotron experiment.

Disclosures

The authors declare no conflicts of interest.

References

1. J. M. Rodenburg, A. C. Hurst, A. G. Cullis, B. R. Dobson, F. Pfeiffer, O. Bunk, C. David, K. Jefimovs, and I. Johnson, "Hard-x-ray lensless imaging of extended objects," Phys. Rev. Lett. **98**(3), 034801 (2007).
2. P. Thibault, M. Dierolf, A. Menzel, O. Bunk, C. David, and F. Pfeiffer, "High-resolution scanning x-ray diffraction microscopy," Science **321**(5887), 379–382 (2008).
3. A. M. Maiden and J. M. Rodenburg, "An improved ptychographical phase retrieval algorithm for diffractive imaging," Ultramicroscopy **109**(10), 1256–1262 (2009).
4. P. Thibault, M. Dierolf, O. Bunk, A. Menzel, and F. Pfeiffer, "Probe retrieval in ptychographic coherent diffractive imaging," Ultramicroscopy **109**(4), 338–343 (2009).
5. Y. Takahashi, A. Suzuki, N. Zettsu, Y. Kohmura, Y. Senba, H. Ohashi, K. Yamauchi, and T. Ishikawa, "Towards high-resolution ptychographic x-ray diffraction microscopy," Phys. Rev. B **83**(21), 214109 (2011).
6. A. Schropp, R. Hoppe, J. Patommel, D. Samberg, F. Seiboth, S. Stephan, G. Wellenreuther, G. Falkenberg, and C. G. Schroer, "Hard x-ray scanning microscopy with coherent radiation: Beyond the resolution of conventional x-ray microscopes," Appl. Phys. Lett. **100**(25), 253112 (2012).
7. J. Vila-Comamala, A. Diaz, M. Guizar-Sicairos, A. Mantion, C. M. Kewish, A. Menzel, O. Bunk, and C. David, "Characterization of high-resolution diffractive x-ray optics by ptychographic coherent diffractive imaging," Opt. Express **19**(22), 21333–21344 (2011).
8. X. Huang, W. Xu, E. Nazaretski, N. Bouet, J. Zhou, Y. S. Chu, and H. Yan, "Hard x-ray scanning imaging achieved with bonded multilayer laue lenses," Opt. Express **25**(8), 8698–8704 (2017).
9. F. Pfeiffer, "X-ray ptychography," Nat. Photonics **12**(1), 9–17 (2018).
10. P. Thibault and A. Menzel, "Reconstructing state mixtures from diffraction measurements," Nature **494**(7435), 68–71 (2013).
11. J. N. Clark, X. Huang, R. J. Harder, and I. K. Robinson, "Dynamic imaging using ptychography," Phys. Rev. Lett. **112**(11), 113901 (2014).
12. X. Huang, K. Lauer, J. N. Clark, W. Xu, E. Nazaretski, R. Harder, I. K. Robinson, and Y. S. Chu, "Fly-scan ptychography," Sci. Rep. **5**(1), 9074 (2015).
13. P. M. Pelz, M. Guizar-Sicairos, P. Thibault, I. Johnson, M. Holler, and A. Menzel, "On-the-fly scans for x-ray ptychography," Appl. Phys. Lett. **105**(25), 251101 (2014).
14. N. Burdet, K. Shimomura, M. Hirose, A. Suzuki, and Y. Takahashi, "Efficient use of coherent x-rays in ptychography: Towards high-resolution and high-throughput observation of weak-phase objects," Appl. Phys. Lett. **108**(7), 071103 (2016).
15. R. Karl, C. Bevis, R. Lopez-Rios, J. Reichanadter, D. Gardner, C. Porter, E. Shanblatt, M. Tanksalvala, G. F. Mancini, M. Murnane, H. Kapteyn, and D. Adams, "Spatial, spectral, and polarization multiplexed ptychography," Opt. Express **23**(23), 30250–30258 (2015).
16. D. J. Batey, D. Claus, and J. M. Rodenburg, "Information multiplexing in ptychography," Ultramicroscopy **138**, 13–21 (2014).
17. C. Bevis, R. Karl, J. Reichanadter, D. F. Gardner, C. Porter, E. Shanblatt, M. Tanksalvala, G. F. Mancini, H. Kapteyn, M. Murnane, and D. Adams, "Multiple beam ptychography for large field-of-view, high throughput, quantitative phase contrast imaging," Ultramicroscopy **184**, 164–171 (2018).
18. L. I. Rudin, S. Osher, and E. Fatemi, "Nonlinear total variation based noise removal algorithms," Phys. D **60**(1-4), 259–268 (1992).
19. R. Horisaki, R. Egami, and J. Tanida, "Single-shot phase imaging with randomized light (spiral)," Opt. Express **24**(4), 3765–3773 (2016).
20. K. Tamasaku, Y. Tanaka, M. Yabashi, H. Yamazaki, N. Kawamura, M. Suzuki, and T. Ishikawa, "SPring-8 RIKEN beamline III for coherent X-ray optics," Nucl. Instrum. Methods Phys. Res., Sect. A **467-468**, 686–689 (2001).
21. J. M. Bioucas-Dias and M. A. T. Figueiredo, "A new twist: Two-step iterative shrinkage/thresholding algorithms for image restoration," IEEE Trans. on Image Process. **16**(12), 2992–3004 (2007).

Optics EXPRESS

22. A. M. Maiden, G. R. Morrison, B. Kaulich, A. Gianoncelli, and J. M. Rodenburg, "Soft x-ray spectromicroscopy using ptychography with randomly phased illumination," Nat. Commun. **4**(1), 1669 (2013).
23. F. Zhang, B. Chen, G. R. Morrison, J. Vila-Comamala, M. Guizar-Sicairos, and I. K. Robinson, "Phase retrieval by coherent modulation imaging," Nat. Commun. **7**(1), 13367 (2016).